Cell Reports
Methods

Article

Stimulated Raman scattering microscopy reveals a unique and steady nature of brain water dynamics

Graphical abstract

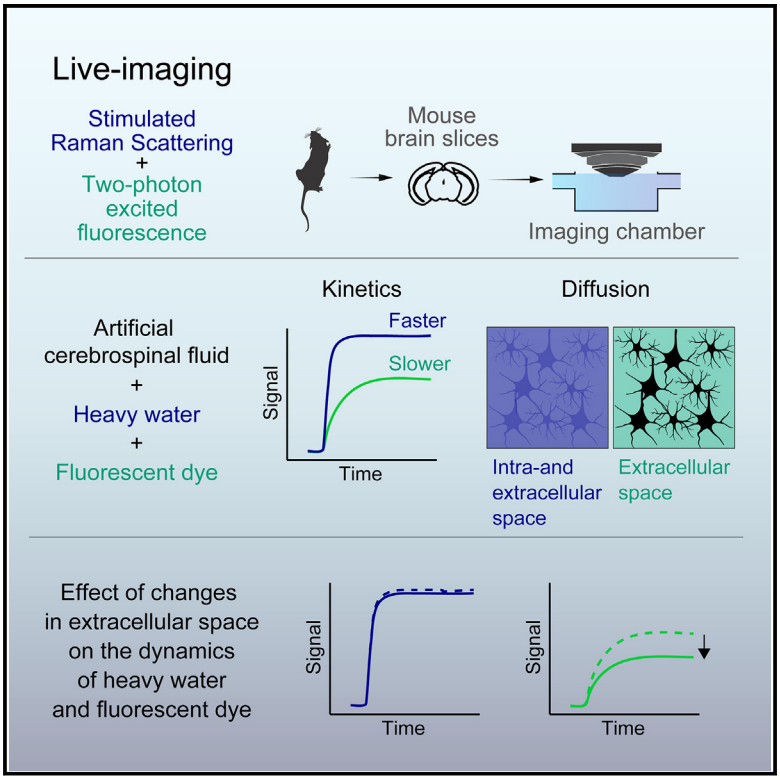

Highlights

- SRS multimodal multiphoton microscopy can visualize water dynamics in brain tissue
- Speed and routes of water diffusion markedly differ from those of fluorescent dyes
- Water dynamics in brain tissues are uniquely steady under different conditions

Authors

Takanori Shinotsuka, Tsuyoshi Miyazawa, Keiko Karasawa, Yasuyuki Ozeki, Masato Yasui, Mutsuo Nuriya

Correspondence

mnuriya@keio.jp

In brief

Shinotsuka et al. develop an SRS microscopy system to characterize the dynamics of water in rodent brain tissues along with the dynamics of fluorescent molecules. Comparisons reveal differences in speed and routes of diffusion between water and dyes and a uniquely steady nature of water dynamics in brain tissues.

Shinotsuka et al., 2023, Cell Reports Methods 3, 100519
July 24, 2023
https://doi.org/10.1016/j.crmeth.2023.100519

CellPress

Cell Reports Methods

CellPress
OPEN ACCESS

Article

Stimulated Raman scattering microscopy reveals a unique and steady nature of brain water dynamics

Takanori Shinotsuka,[1] Tsuyoshi Miyazawa,[1] Keiko Karasawa,[1] Yasuyuki Ozeki,[2] Masato Yasui,[1] and Mutsuo Nuriya[1,3,4,5,*]
[1]Department of Pharmacology, School of Medicine, Keio University, 35 Shinanomachi, Shinjuku, Tokyo 160-8582, Japan
[2]Department of Electrical Engineering and Information Systems, The University of Tokyo, Tokyo 113-8656, Japan
[3]Graduate School of Environment and Information Sciences, Yokohama National University, 79-1 Tokiwadai, Hodogaya, Yokohama, Kanagawa 240-8501, Japan
[4]Precursory Research for Embryonic Science and Technology (PRESTO), Japan Science and Technology Agency (JST), 4-1-8 Honcho, Kawaguchi, Saitama 332-0012, Japan
[5]Lead contact
*Correspondence: mnuriya@keio.jp
https://doi.org/10.1016/j.crmeth.2023.100519

MOTIVATION The characterization of water dynamics in brain tissues is critical for understanding all chemical reactions occurring in healthy and diseased brains; however, there is no imaging technique currently available to directly image water dynamics in brain tissues at cellular resolution. Therefore, we developed a multimodal multiphoton microscope to overcome this problem and applied it to brain tissues. Stimulated Raman scattering allows for direct visualization of water dynamics in brain tissues at cellular resolution, and the simultaneously acquired two-photon fluorescence signals allow for side-by-side comparison of water and solute dynamics.

SUMMARY

The biological activities of substances in the brain are shaped by their spatiotemporal dynamics in brain tissues, all of which are regulated by water dynamics. In contrast to solute dynamics, water dynamics have been poorly characterized, owing to the lack of appropriate analytical tools. To overcome this limitation, we apply stimulated Raman scattering multimodal multiphoton microscopy to live brain tissues. The microscopy system allows for the visualization of deuterated water, fluorescence-labeled solutes, and cellular structures at high spatiotemporal resolution, revealing that water moves faster than fluorescent molecules in brain tissues. Detailed analyses demonstrate that water, unlike solutes, diffuses homogeneously in brain tissues without differences between the intra- and the extracellular routes. Furthermore, we find that the water dynamics are steady during development and ischemia, when diffusions of solutes are severely affected. Thus, our approach reveals routes and uniquely robust properties of water diffusion in brain tissues.

INTRODUCTION

Water constitutes nearly 80% of tissue weight and is the most predominant molecule in the brain. Because water is the common solvent for most bioactive molecules, homeostasis of water is critical in maintaining all chemical reactions and thereby the physiological functions of the brain. Indeed, the amount of water in the brain as a whole is under tight homeostatic control, and slight changes in brain water content result in severe outcomes; various cognitive dysfunctions can be induced by a small percentage change in brain water content, and lethality can result from a change in water content of approximately 10%.[1] In addition, the clinical diagnoses of various neurological diseases can be made on the basis of water detected using diffusion-weighted magnetic resonance imaging (MRI).[2] Although the importance of water homeostasis at the whole-tissue level is well established, little is known about water dynamics at the cellular and subcellular levels, which form the physiological and pathophysiological bases for the macroscopic behavior of water in the brain,[3] due to the lack of appropriate analytical tools. Thus, the first step to fill in the large missing piece and facilitate our understanding of brain physiology and pathophysiology is to establish a system through which dynamic water movements in brain tissues can be directly visualized and characterized at cellular resolution.

Fluorescence imaging is one of the most widely used imaging techniques in biology. Indeed, fluorescent dye-based analyses have been utilized to characterize the dynamics of molecules in brain tissues.[4–6] However, commonly used fluorescent dyes have molecular weights of >500; hence, it is inappropriate to tag and trace small bioactive molecules, including water, using

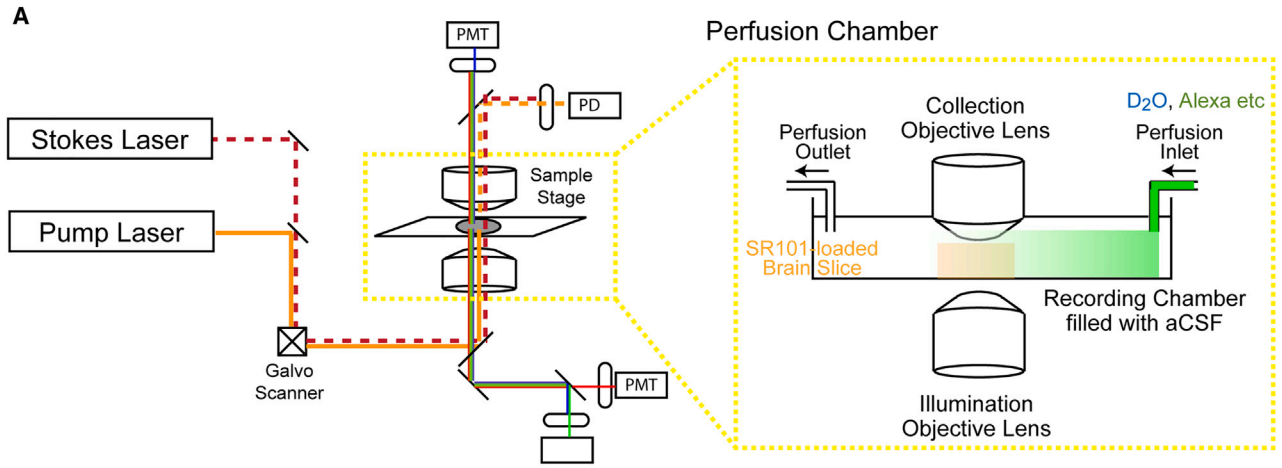

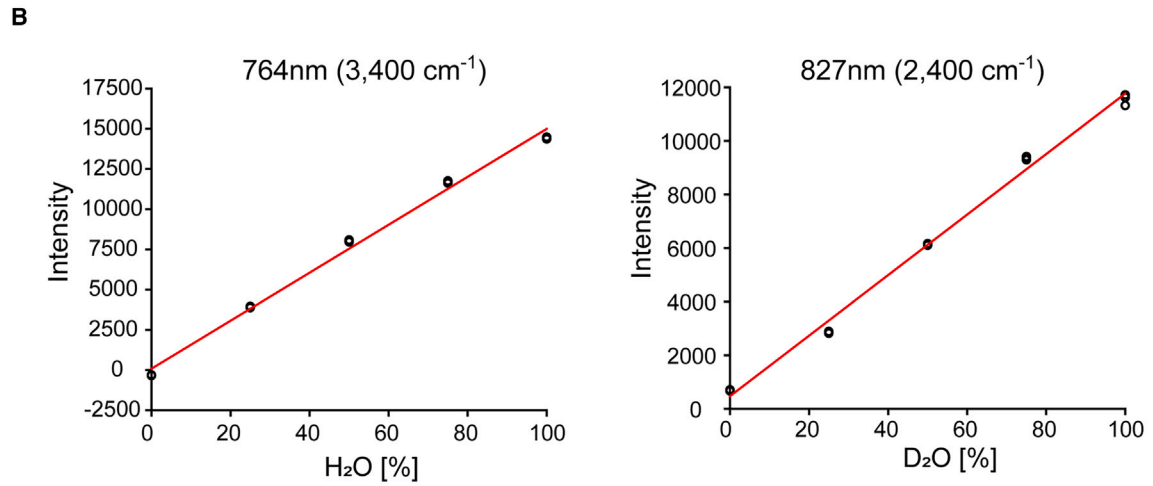

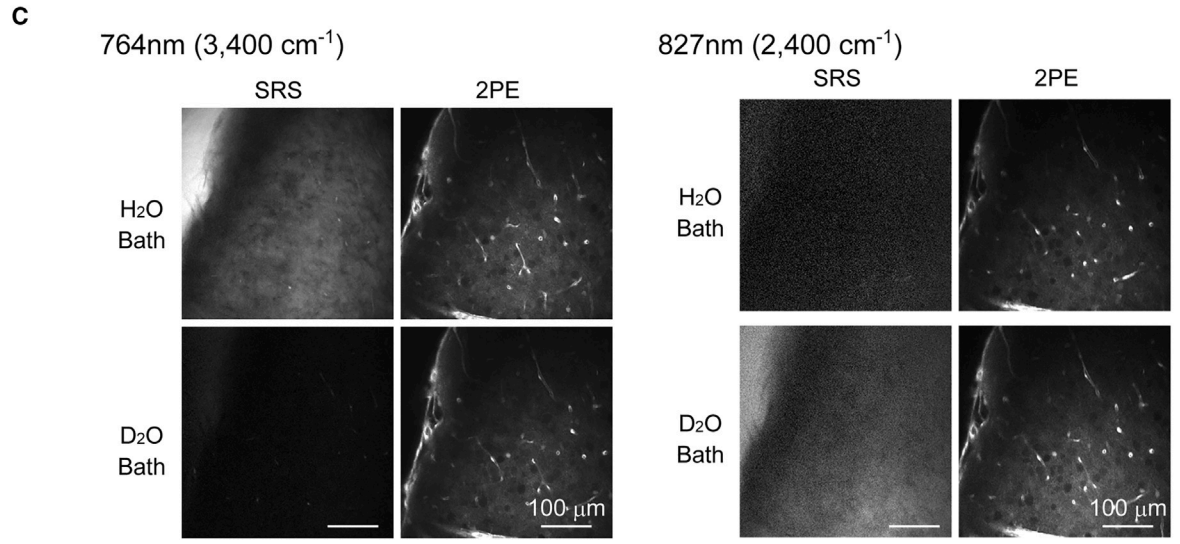

(legend on next page)

fluorophores. In other disciplines, various optical phenomena other than fluorescence have been utilized for analyses. Among them, Raman scattering has great potential for the imaging of small bioactive molecules. The introduction of small Raman-active and distinguishable Raman tags allows for the identification and imaging of small bioactive molecules that cannot be labeled with fluorophores.[7–10] Furthermore, although poor sensitivity has hampered the application of spontaneous Raman scattering microscopy in biology, coherent Raman scattering, such as coherent anti-Stokes Raman scattering and stimulated Raman scattering (SRS), dramatically increases signal intensity, thereby permitting a real-time Raman imaging of biological samples.[11] Coherent Raman scattering imaging has additional advantages for brain imaging; it utilizes the nonlinear optical effect of near-infrared photons and thus elicits an inherent tissue-sectioning capacity, even deep inside tissues, akin to two-photon excitation fluorescence (2PE) microscopy, which is currently widely used in biology. Furthermore, when appropriately designed, ultrashort pulsed lasers used for coherent Raman scattering microscopy can induce other nonlinear optical effects, including the two-photon excitation of fluorophores. Such multimodal multiphoton microscopy allows for multifaceted analyses of complicated biological phenomena.[12,13]

Thus, in this study, we applied coherent Raman scattering microscopy to brain slices and characterized water dynamics in brain tissues by tracking Raman-tagged deuterated water (D_2O). The simultaneous excitation of fluorophores characterizes the dynamics of water and solutes inside brain tissues at a high spatiotemporal resolution. This multimodal multiphoton microscopy reveals the unique properties of water dynamics in brain tissues, which cannot be inferred from solute properties.

RESULTS

Multimodal multiphoton imaging of water in brain tissues

To visualize water in brain tissue, we developed a multimodal multiphoton microscopy system with SRS imaging ability[10] (Figures 1A and S1A). The system utilizes highly tissue-penetrating near-infrared picosecond pulsed lasers with nonlinear optical effects that limit the effective focal volume; therefore, the system is expected to allow for high-spatial-resolution imaging deep in the tissues. In addition, our SRS system enables a simultaneous excitation of fluorescent molecules, thereby permitting a multimodal imaging of fluorophores.[10] Importantly, SRS signal collection is based on the detection of incident laser modulation and not the collection of newly generated photons with a particular wavelength, similar to 2PE; hence, there are no concerns regarding signal overlaps or contamination of SRS and fluorescence. This permits completely independent and simultaneous imaging of solvents, solutes, and/or cellular markers.

To monitor the dynamics of water, we utilized the isotope effect; the replacement of normal water (H_2O) with D_2O should be monitored by observing the O-D and O-H vibration modes. As a first step, we examined the ability of our system to distinguish H_2O from D_2O using the solution samples. Subsequently, we found a near-linear relationship between the solution's H_2O concentration and the SRS signal intensity measured at the vibration frequency of O-H (3,400 cm^{-1}) and the D_2O concentration and the SRS signal intensity at the vibration frequency of O-D (2,400 cm^{-1}) (Figures 1B and S1B).[14] Note that our system utilizes a 1,032-nm fixed-wavelength laser as a Stokes beam and a tuned single-wavelength laser from an optical parametric oscillator (OPO) as a pump beam, so that it can visualize one wave number of SRS signal at a time, and these measurements were performed independently. Thereafter, we evaluated whether this H_2O-D_2O discrimination occurs in brain slices. First, fixed brain tissues prepared from mice expressing enhanced green fluorescent protein (EGFP) under the CAG promoter (cytomegalovirus immediate early (CMV-IE) enhancer, chicken beta-actin promoter, and rabbit beta-globin genomic DNA) were visualized in H_2O or D_2O at 3,400 and 2,400 cm^{-1}. Equally intense EGFP 2PE signals were readily collected under both 3,400 and 2,400 cm^{-1} SRS imaging conditions and served as localization markers. In contrast to EGFP signals, high contrasts of H_2O and D_2O were observed in the brain tissues by SRS imaging (Figure 1C). Therefore, these findings demonstrate that this multimodal multiphoton microscopy system can be used to visualize and distinguish H_2O and D_2O in brain tissues. The use of brain slices facilitates a rapid exchange of extracellular solution from a pure H_2O-based solution to a D_2O-containing solution; thus, it may be possible to track the exchange of these solutions and hence characterize the dynamics of water in brain tissues.

Dynamics of solutes and water in living brain tissues

To characterize water dynamics in living brain tissues, 300-μm-thick acute cortical slices prepared from mice were placed in an imaging chamber with continuous perfusion of an oxygenated external solution. Considering the suggested roles of astrocytes that express high levels of water channel aquaporin 4 (AQP4) in the regulation of brain water dynamics,[15] we imaged astrocytes in brain tissue using the astrocyte marker sulforhodamine 101 (SR101).[16] When the observation areas were determined, a D_2O-containing external solution was introduced into the imaging chamber through a perfusion system in the middle of 5–10 min of time-lapse imaging (Figure 1A). To understand the nature of water dynamics, it is crucial to have a reference and

Figure 1. Multimodal multiphoton imaging of water in brain tissues

(A) Schematic diagram of the system. The right shows a close-up view of the imaging chamber.

(B) SRS detection of H_2O- and D_2O-based solutions. SRS measurements were performed on the water with different combinations of H_2O and D_2O at O-H and O-D vibration modes (3,400 and 2,400 cm^{-1}, respectively).

(C) Multimodal multiphoton detection of fixed brain slices in H_2O and D_2O. Fixed brain slices prepared from CAG-EGFP mice were soaked in H_2O or D_2O to equilibrium and visualized using multimodal multiphoton microscopy tuned to O-H or O-D vibration modes. Simultaneously obtained 2PE signals of EGFP are also shown. 2PE, two-photon excitation fluorescence; aCSF, artificial cerebrospinal fluid; EGFP, enhanced green fluorescent protein; SRS, stimulated Raman scattering; SR101, sulforhodamine 101; PMT, photomultiplier tube; PD, photodiode. See also Figure S1.

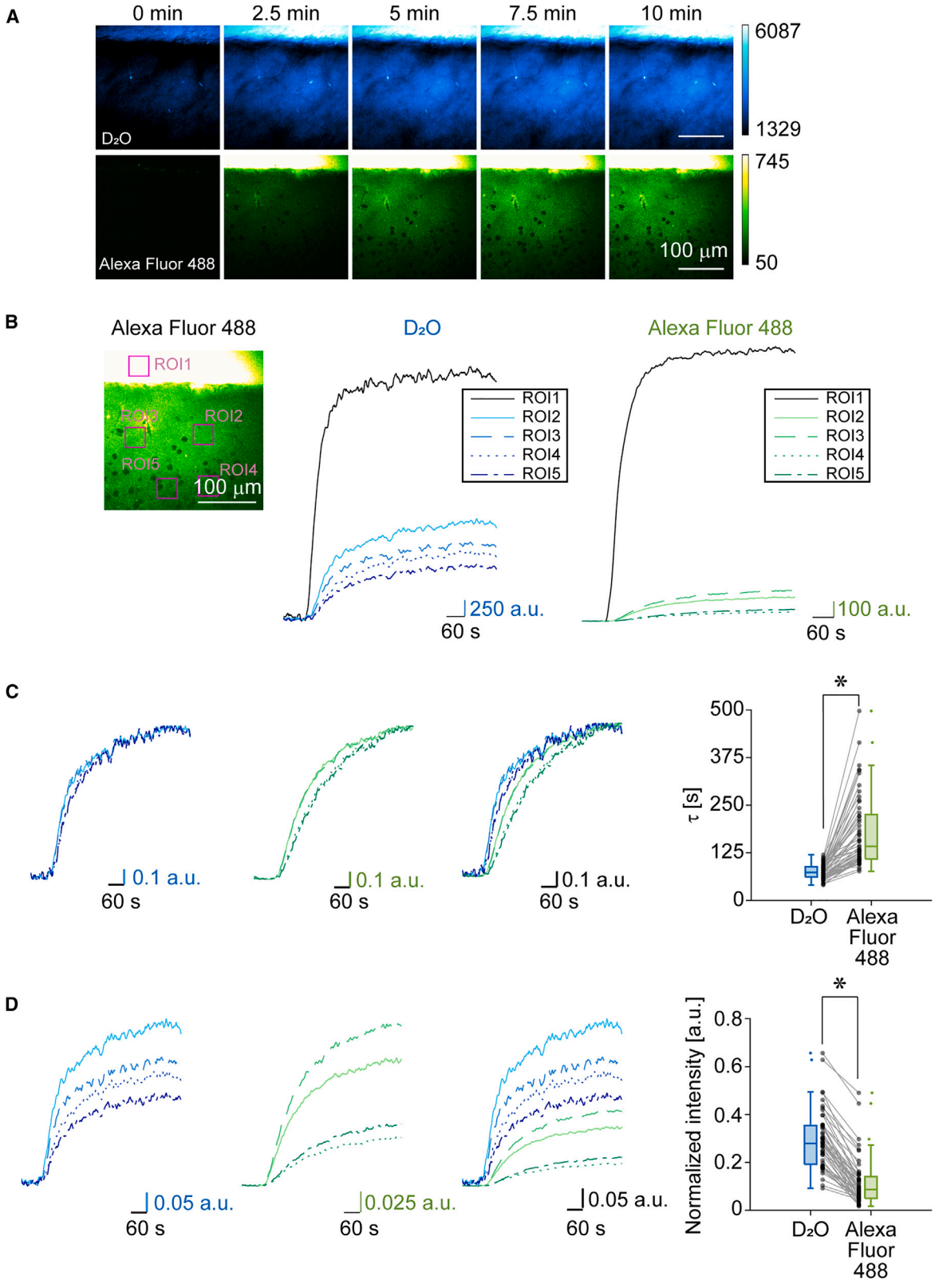

(legend on next page)

compare them in a side-by-side manner. In this regard, Alexa Fluor 488 dye is ideal, because it has been widely used as a representative water-soluble solute to characterize diffusion dynamics of molecules in brain tissues.[4–6] Thus, Alexa Fluor 488 carboxylic acid (molecular weight 725.84) was introduced as a solute, together with D_2O for simultaneous detection (Figure 1A). To minimize the potential biological effects of the introduction of D_2O into the system, the concentration of D_2O was reduced to 20% of the total water content, which was shown to have a minimum effect, if any, on cells and tissues.[17] Multichannel time-lapse imaging was performed to continuously and simultaneously monitor the diffusion dynamics of water and solutes. The imaging was performed at 1.1 Hz in an ~400 × ~400 μm area with lateral and axial resolutions of 0.65 and 6.2 μm, respectively (see discussion for details). The laser power of the pump and Stokes beams was set to 75–125 mW under an objective lens, at which no apparent phototoxicity was observed. To accurately evaluate their spatiotemporal dynamics, random drifts in the location of the brain slice during imaging were corrected based on the SR101 images (Figure S2A). When a fluorophore-containing D_2O-based external solution was introduced, immediate changes in the signals of D_2O-SRS as well as Alexa Fluor 2PE in the bath were observed outside the brain slices (Figures 2A and 2B). In contrast, we found that the arrival of both D_2O and Alexa Fluor dye was slower inside than outside the brain tissues; we observed a gradual and delayed diffusion of dye and D_2O from the pial surface toward the deeper layers in brain slices (Figures 2A and 2B; Videos S1 and S2). Thus, this system enables simultaneous visualization of the dynamics of water and solutes in brain tissues.

For quantitative analyses, the signal intensity changes in D_2O and Alexa Fluor dye were fitted with an exponential function to calculate the time constant of the fluxes (Figures S2B–S2D). Generally, the signal changes reached a plateau within 5–10 min of time-lapse imaging with a time constant of tens of seconds for both water and Alexa Fluor dye. This analysis revealed a positive correlation between the distance from the pial surface and the time constant, confirming that the system allows for quantitative analyses of water and dye movements in brain tissues (Figures S3A and S3B). This finding demonstrates that, while molecules (D_2O and Alexa Fluor dye) can diffuse into brain tissues not only from the pial surface but also from the lateral area of sectioned brain slices, the contribution of the latter is small, and directional movement of molecules from the pial surface to deeper layers of cortical areas can be evaluated under our experimental conditions. Notably, a side-by-side comparison between water and Alexa Fluor dye demonstrated that water diffusion into the brain tissue is faster than that of the dye molecule (Figure 2C), demonstrating the ability of this imaging platform to reveal the unique features of water dynamics that cannot be assessed by an indirect measurement of fluorophore dynamics.

Generally, it is assumed that most water-soluble molecules, such as Alexa Fluor 488, move inside brain tissues through the extracellular space,[4–6] which restricts the movement of molecules through the narrow space as well as the tortuosity of the extracellular space.[18] Thus, we hypothesized that differences in the speed of diffusion in brain tissues may be further exemplified using larger molecules. To test this hypothesis, the same comparison was applied to a dye with a larger molecular weight, namely, Alexa Fluor 488 dye conjugated to a 10-kDa dextran (Figure 3). This analysis revealed that the difference between the speeds of influx of water and solutes was greater for the 10-kDa dextran-conjugated Alexa Fluor 488 (Figure 3C), consistent with the idea that the diffusion of large-sized molecules is more hindered in brain tissues compared with smaller molecules.[19] Considering that fluorescent proteins have larger molecular weights than 10-kDa dextran, our findings further demonstrate the importance of a direct visualization of water, instead of speculation from indirect methods of fluorophore imaging, for the characterization of water dynamics in brain tissues.

Distribution of water and solutes inside brain tissues

One of the most critical unresolved issues in considering the dynamics of water is its routes of diffusion in brain tissues at the cellular/subcellular levels.[3] To address this point, we took advantage of the high spatial resolution of nonlinear optical microscopy and analyzed the spatial patterns of D_2O and Alexa Fluor 488 in more detail. By comparing images taken before and after the introduction of D_2O and Alexa Fluor 488, we evaluated the spatial distribution of D_2O and Alexa Fluor 488 in the brain tissues. Alexa Fluor 488 images clearly showed dark areas (shadows) corresponding to the intracellular regions, the most prominent of which were somata of large-diameter neurons[5,6] (Figure 4A). However, differences between intra- and extracellular regions were not evident in D_2O SRS images (Figures 4A and S4A). This difference between the dye and the D_2O can be clearly observed in the quantitative results (Figure 4B). The separation of intra- and extracellular spaces becomes less stringent in cells with smaller diameters due to the limited spatial resolution of the system (see discussion); nevertheless, differences between the diffusion of water and that of the fluorophore were still evident for SR101-positive astrocytes (Figures 4C and S4B). These observations demonstrate that water molecules diffuse into cells, in contrast to water-soluble fluorophores, which are nearly indistinguishable from those outside cells on a timescale of tens of seconds. These differential dynamics of water and fluorophores demonstrate that the volume fraction occupied by newly introduced D_2O is higher than that of dyes. Indeed, when the intensities of D_2O SRS and fluorophore 2PE signals

Figure 2. Dynamics of solutes and water in living brain tissues

(A) Representative images of D_2O and Alexa Fluor 488 influx into brain tissues.

(B) Representative traces of D_2O and Alexa Fluor 488 signals at different ROIs shown on the left.

(C) Comparison of speed of diffusion into brain tissues between D_2O and Alexa Fluor 488. All traces are normalized to their final values to readily visualize the differences in diffusion kinetics. The right shows the summary data (n = 52 ROIs from six slices; *$p = 3.5 \times 10^{-10}$, Wilcoxon signed-rank test).

(D) Comparison of signal intensities of D_2O and Alexa Fluor 488. Traces are normalized to the value of ROI 1 (outside solution) to compare relative intensities; the right shows the summary of all data (n = 52 ROIs from six slices; *$p = 3.5 \times 10^{-10}$, Wilcoxon signed-rank test). ROI, region of interest. See also Figures S2 and S3.

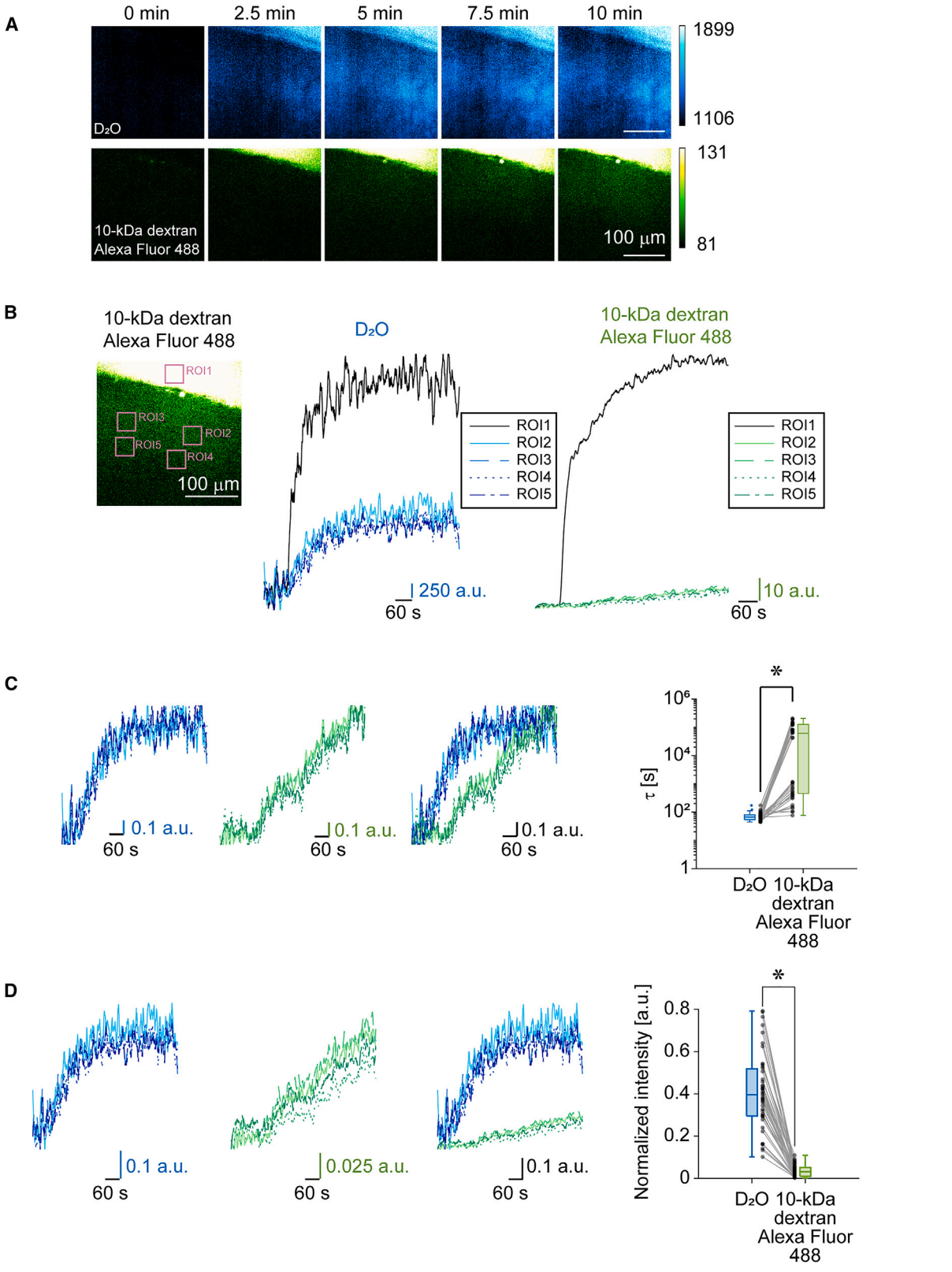

(legend on next page)

inside brain tissues were compared with those outside, the former was larger than the latter (Figures 2D and 3D). Therefore, differences between water dynamics in the extra- and intracellular spaces are indistinguishable in minutes or longer timescales inside the brain tissue. Thus, water is clearly distinguished from water-soluble solutes by its spatial dynamics; consequently, water and water-soluble solutes may behave differently under physiological and/or pathophysiological conditions.

Dynamics of water and solutes at different developmental stages

Finally, we examined water dynamics under different conditions to evaluate the robustness of brain tissue water dynamics. During development, especially during the neonatal period, brain water content gradually decreases with simultaneous extracellular space reduction, resulting in more restricted solute dynamics.[18,20] However, whether such changes are accompanied by alterations in water dynamics remains unknown. Thus, we performed diffusion analyses in brain slices prepared from mice in early (approximately 1-week-old mice, postnatal day 7–10 (P7–P10); Figures 5A and 5C) and later (approximately 3-week-old mice, P21–P25; Figures 5B and 5D) developmental stages. Mice typically open their eyes at approximately 2 weeks of age, and therefore the visual cortex used in this study underwent dramatic changes in the quality and quantity of synaptic connections, leading to changes in tissue cellular organization.[21] Consistent with previous reports, we confirmed that dye molecules move more slowly and in smaller quantities in older animals than in younger animals, suggesting a reduced volume and an increased tortuosity of the extracellular space (Figures 5F, 5H, and 5J). Note that all measurements were performed in cortical areas without significant differences in distance from the cortical surface between groups (Figure S3C). In contrast, we did not find significant differences in water dynamics between the two different developmental stages, thereby revealing the uniquely robust and steady nature of brain tissue water dynamics during development, presumably due to the unique ability of water to diffuse through both intra- and extracellular compartments (Figures 5E, 5G, and 5I).

Dynamics of water and solutes under a pathological condition

Furthermore, we examined water dynamics under pathological conditions. Clinically, diffusion-weighted MRI has revolutionized the early detection of brain pathologies, such as ischemia. Changes in diffusion-weighted MRI signals under pathological conditions are considered to reflect macroscopic changes in brain water diffusion; however, the underlying microscopic molecular picture remains poorly understood.[2,22] Specifically, a generally assumed model in which water is redistributed from the extracellular space, where it is relatively diffusible, to diffusion-limited intracellular compartments requires experimental examination. Thus, to test the validity of this model and gain insights into the pathophysiology of brain ischemia, we employed a slice model to mimic a pathological condition—oxygen-glucose deprivation (OGD)[23]—and evaluated water dynamics under this condition.

Water and Alexa Fluor 488 dynamics were analyzed before and after 30 min of OGD (Figures 6A and 6C) or for 30 min under the normal condition (i.e., with oxygen and glucose supply), as a control (Figures 6B and 6D). As expected, we found a severely reduced influx of Alexa Fluor 488 into brain tissues under OGD, reflecting cell swelling that resulted in a reduction of the extracellular space, the only route for dye diffusion into brain tissues (Figures 6E, 6F, and 6H). Again, note that all measurements were performed in cortical areas without significant differences in distance from the cortical surface between groups (Figure S3D). Notwithstanding, no significant changes in water diffusion were observed under OGD, thereby revealing the extremely robust and steady nature of water diffusion under pathological conditions (Figures 6E, 6F, and 6G). This finding is consistent with the stability of water dynamics during development, presumably supported by the global diffusion of brain tissue water through both intra- and extracellular spaces. Hence, these findings do not support the generally assumed idea that changes in diffusion-weighted MRI signals under ischemic conditions reflect static water redistribution from the extracellular to the intracellular space; the findings suggest other mechanisms, potentially including pulsation-mediated changes, in the active transport of water. Regardless of the precise mechanisms, these results reveal the unique and steady nature of brain tissue water dynamics under ischemic conditions. Therefore, we found that water diffusion into and out of brain tissues is stable, even during considerable tissue changes that substantially alter solute diffusion behavior.

DISCUSSION

In this study, we applied SRS multimodal multiphoton microscopy to live brain tissue to characterize the dynamics of water (D_2O) and solutes (Alexa Fluor 488) in brain tissues at high spatiotemporal resolution. Detailed analyses reveal a faster flow of water molecules compared with solutes, supported by its diffusion via both intra- and extracellular spaces. Finally, we demonstrated a uniquely robust and steady nature of water dynamics in both physiological and pathological conditions, when that of solutes is severely affected. These results not only reveal the unique nature of water dynamics but also warrant the need for

Figure 3. Dynamics of large-sized solutes and water in brain tissues

(A) Representative images of D_2O and 10-kDa dextran-conjugated Alexa Fluor 488 influx into brain tissues.

(B) Representative traces of D_2O and 10-kDa dextran-conjugated Alexa Fluor 488 signals at different ROIs.

(C) Comparison of the speed of diffusion into brain between D_2O and 10-kDa dextran-conjugated Alexa Fluor 488. All traces are normalized to their final values to readily visualize the differences in diffusion kinetics; the right shows the summary of all the data (n = 43 ROIs from six slices; *$p = 1.1 \times 10^{-8}$, Wilcoxon signed-rank test).

(D) Comparison of influxes of D_2O and 10-kDa dextran-conjugated Alexa Fluor 488. Traces are normalized to those of ROI 1 (outside solution) to compare relative intensities; the right shows the summary of all the data (n = 43 ROIs from six slices; *$p = 1.2 \times 10^{-8}$, Wilcoxon signed-rank test).

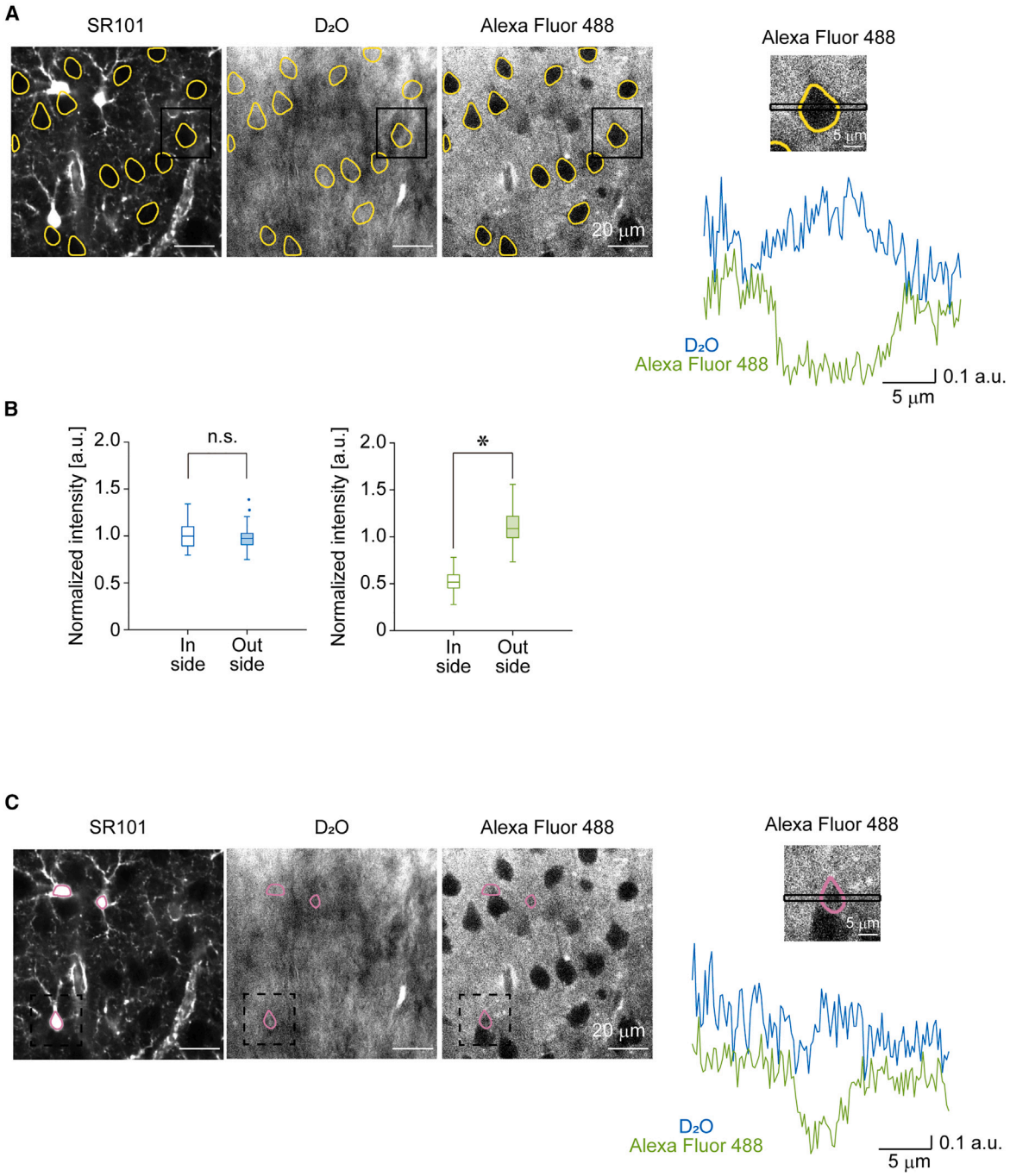

Figure 4. Distribution of water and solutes inside brain tissues

(A) Representative images of D_2O and Alexa Fluor 488 dye. Images of the astrocyte marker SR101, D_2O, and Alexa Fluor 488 are shown. Yellow circles represent automatically drawn shapes of cells extracted from shadow images of Alexa Fluor 488. The right shows an enlarged image of the selected area indicated in the left images and the intensity profiles across the boxed area (blue, D_2O; green, Alexa Fluor 488).

(B) Comparison between intensities of D_2O SRS and Alexa Fluor 488 2PE signals inside and outside cells. Intensities of ROIs inside and outside these cells, as defined in the yellow circles in (A), were plotted (n = 54 ROIs from five slices) for D_2O SRS (n.s., $p = 4.4 \times 10^{-1}$, Brunner-Munzel test) and Alexa Fluor 488 2PE signals (*$p = 2.1 \times 10^{-171}$, Brunner-Munzel test).

(C) Analysis of D_2O and Alexa Fluor 488 intensities inside and outside astrocytes. Sites of astrocytes were defined based on the SR101 image; the intensity profiles of the selected area are shown (blue, D_2O; green, Alexa Fluor 488). See also Figure S4.

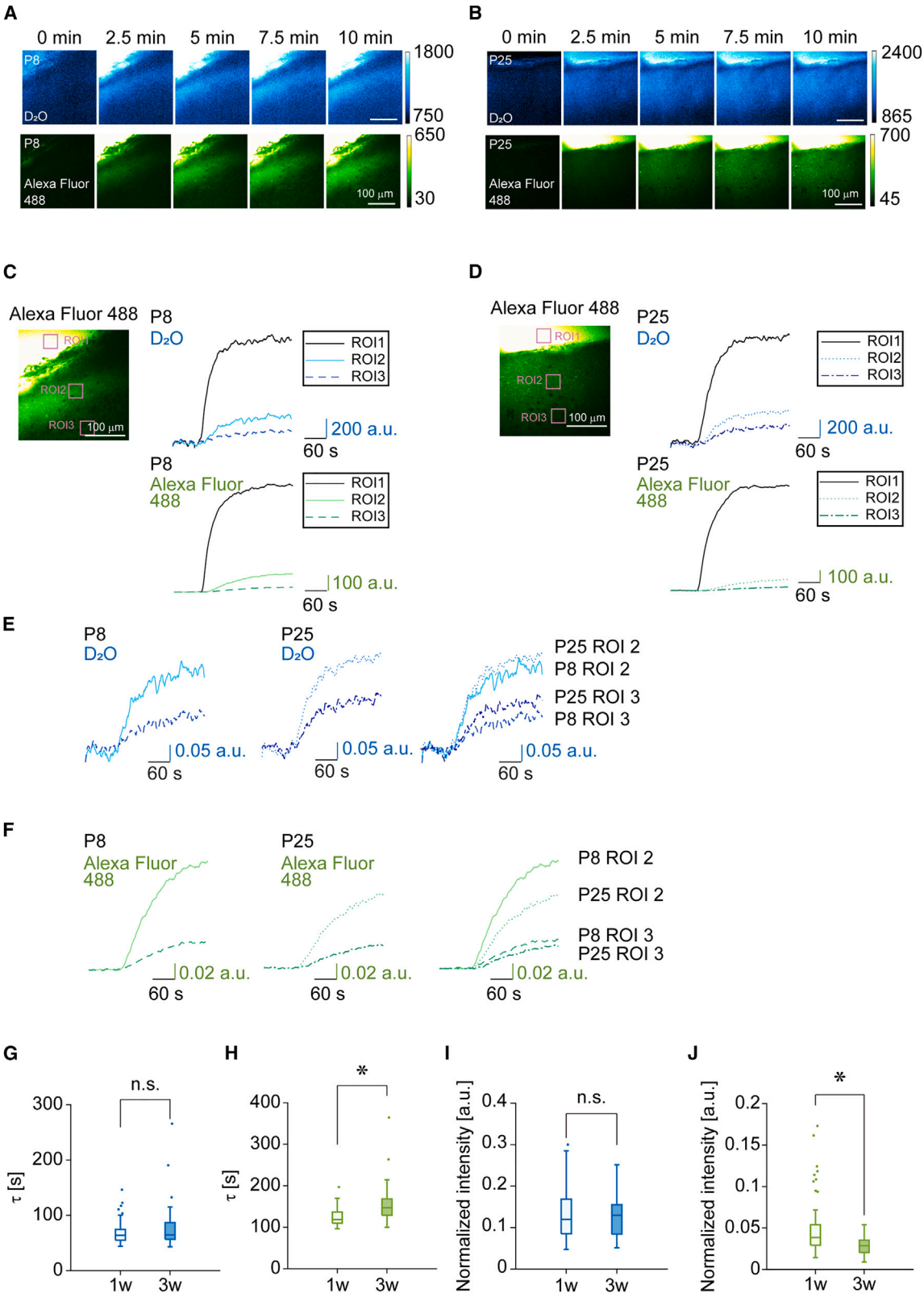

(legend on next page)

direct visualization of water for its characterization in brain tissues.

Taking advantage of this unique system, we investigated brain tissue water and solute dynamics. Detailed analyses clearly demonstrated key differences between the dynamics of water and fluorophores; water diffuses faster and homogeneously inside brain tissues, whereas fluorescent dyes diffuse more slowly and specifically outside cells, showing nonhomogeneous distributions. We did not observe differentially regulated water movement in brain tissues; water appeared to diffuse into the deep layers of brain tissues without preferential routes (e.g., extracellular versus intracellular space) or cell types (e.g., neurons versus astrocytes), making the dynamics of water unique. However, this does not mean that water movements inside and outside the cells, as well as through the plasma membrane, are completely equal. Instead, it means that the differences in water movements, if any, are not distinguishable in the temporal domain of seconds and the spatial resolution of approximately 0.5 μm, which are high enough to enable the detection of water movements in brain tissues in cellular contexts. Furthermore, it should be noted that, although we can compare parameters obtained under different conditions within this study (e.g., normal versus OGD), these values cannot be directly compared with those obtained in other studies. This is due to critical differences in the experimental design among studies; probes were applied continuously in bulk solution in this study, while commonly performed diffusion measurements employ pulsative application of probes from a point source. To compare parameters taken from different experimental paradigms, the construction of specialized theory, novel numerical simulation, and diffusion experiments need to be combined. Although it is beyond the scope of this study, such future efforts are awaited to further evaluate the physical nature of water diffusion inside brain tissues.

Moreover, our data showing no differences between water dynamics between neurons and astrocytes do not appear to support the roles of AQP4, a specialized water channel specifically expressed in astrocytes and enriched at their endfeet. This point is further suggested by the similar spatial patterns of D_2O distribution in brain slices prepared from wild-type and AQP4-knockout animals (Figures S4C and S4D). However, the potential roles of AQP4 should be interpreted cautiously from our data; the series of analyses in this study can be used to evaluate the routes of passive water diffusion that are determined by resistance to water movement inside brain tissues. This resistance results from multiple factors, such as local diffusion barriers created by cellular and subcellular structures. Obviously, the presence of AQP4 should reduce the resistance of the plasma membrane, as previously demonstrated using cultured HeLa cells.[24] Meanwhile, the same study revealed a rapid influx of water into cells via AQP4-independent routes, including passive diffusion through the lipid bilayer and other channels, that allow water to cross the plasma membrane with a time constant of ~100 ms.[25] Thus, we speculate that innate plasma membrane water permeability is sufficient to support the global flux of water inside brain tissues we report in this study, which takes place over long distances (hundreds of micrometers) in tens of seconds. The presence of AQP4 may facilitate water diffusion through the plasma membrane in situations where a specific pressure for water flux exists, and therefore, fast transport of large quantities of water molecules needs to be achieved. Potential mechanisms of such pressure include pulsation-dependent vascular changes and constant differences in osmolality inside brain tissues. Future studies are required to characterize these potential active transport mechanisms.

Some technical aspects should be considered when interpreting our results. First, the absolute SRS signal intensity at a particular point in the field of view of the imaging system is subject to pump and Stokes laser intensities. In the thick tissue samples used in this study, the laser intensities at focal points are affected by biological materials with different refractive indices that exist outside the focal plane in the optical path of lasers, which is variable in each position; therefore, the absolute values of SRS signal intensities cannot be simply interpreted as the concentration of water. This may also lead to nonhomogeneous signal distributions of D_2O in brain tissues, as shown in Figure 4. Indeed, the global tendencies of uneven SRS signal intensities in the fields of view were found to be similar at 3,400 (O-H stretch region) and 2,900 cm^{-1} (C-H stretch region), although they were clearly different at the cellular and subcellular levels (Figure S5A). Moreover, such nonhomogeneous signal patterns almost disappear when the samples are treated for tissue-clearing procedures that equalize the refractive indices inside tissues with those of the medium[26] (Figure S5B). Nevertheless, the linear relationship between the SRS signals and the target molecule's concentration remains at each position; hence, we assessed the speed and extent of water dynamics using the normalized SRS signal intensity obtained from O-H to O-D solution exchange.

Second, although it is far superior to spontaneous Raman scattering, the sensitivity of SRS is substantially lower than that of fluorescence. Therefore, concentrations of molecules to be observed by Raman (D_2O in this study) need to be higher compared with fluorescent molecules. Although this does not affect the diffusion properties of molecules, combination of the above-mentioned optical inhomogeneity of samples, differences

Figure 5. Dynamics of water and solutes at different developmental stages

(A–D) Representative images (A and B) and traces (C and D) of D_2O and Alexa Fluor 488 diffusion into brain slices prepared from animals at postnatal day 8 (P8) (A and C) and P25 (B and D).

(E and F) Comparison between D_2O diffusion (E) and Alexa Fluor 488 (F) in mice at P8 and P25. For comparison, the traces are normalized to outside signals (ROI 1) in each condition.

(G and H) Summary of the diffusion time constants of D_2O (G; n.s., $p = 7.6 \times 10^{-1}$, Brunner-Munzel test) and Alexa Fluor 488 (H; $^*p = 3.9 \times 10^{-6}$, Brunner-Munzel test) obtained from 1- and 3-week-old animals (1 week old, n = 56 ROIs from 10 slices; 3 weeks old, n = 43 ROIs from 10 slices).

(I and J) Summary of the normalized intensities of D_2O (I; n.s., $p = 2.8 \times 10^{-1}$, Brunner-Munzel test) and Alexa Fluor 488 (J; $^*p = 3.4 \times 10^{-6}$, Brunner-Munzel test) obtained from 1- and 3-week-old animals (1 week old, n = 56 ROIs from 10 slices; 3 weeks old, n = 43 ROIs from 10 slices).

See also Figure S3. Scale bars, 100 μm.

CellPress
OPEN ACCESS

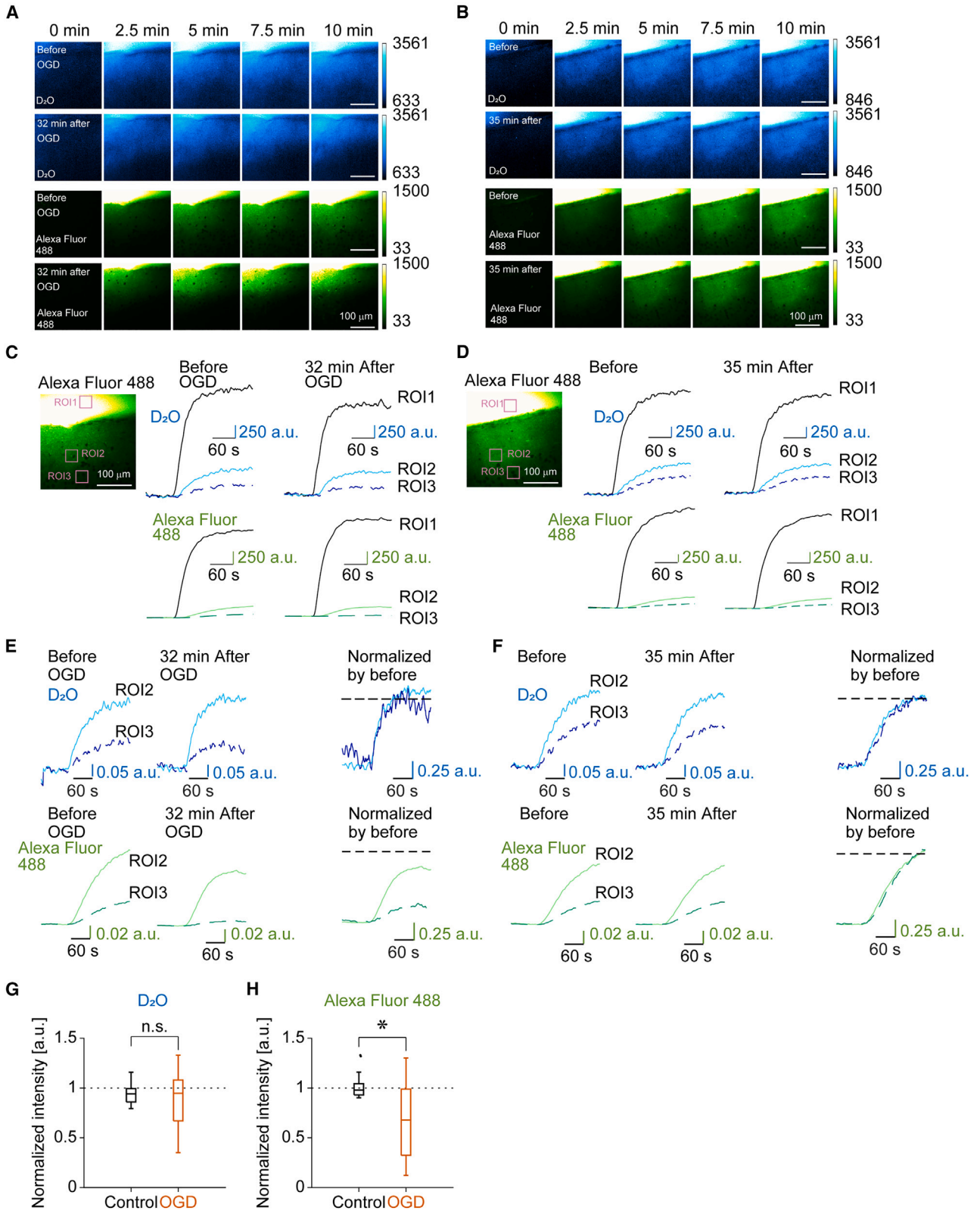

(legend on next page)

in sensitivities among different modalities, differences in concentrations of target molecules, and other factors define the sensitivity at each position and thereby may affect "apparent arrival time" of the target molecules in diffusion analyses. Therefore, as performed in this study, detailed data analyses with curve fitting as well as corrections for sample movements are warranted.

Finally, the spatiotemporal resolution of our system should be considered when interpreting our experimental results. Nonlinear optical microscopy has a high three-dimensional spatial resolution, especially compared with other water imaging modalities, such as MRI.[27] We used subresolution-sized alkyne beads to estimate the spatial resolution of our SRS system defined by the full width at half-maximum (FWHM) to be approximately 0.65 and 6.2 μm for lateral and axial axes, respectively (Figure S5C). This resolution is high enough to completely separate signals from large neuron cell bodies from those outside neurons; numerical simulations indicate that less than 1% of signal contaminations occur from outside at the center of a 20-μm-diameter cell body (Figure S5D). However, outside these large cell bodies, a myriad of small-diameter neurites and glial processes exist, which cannot be separated by the spatial resolution of our system or by other standard optical microscopies. In fact, the same simulations indicate that nearly 50% of signal contaminations occur from outside areas at the center of a 5-μm-diameter sphere. Therefore, signals observed in "extracellular" regions originate from both extra- and intracellular spaces of these small processes. Nevertheless, a clear observation of shadow images via 2PE of cell bodies and the distinction of fluorescence signals of cell bodies and other areas demonstrated that our analysis can be used to distinguish between intra- and extracellular diffusion of molecules, including water. In fact, when the same diffusion analyses were performed using agarose gel with small-sized materials that were expected to lower the diffusion of water (synthetic crystalline aluminosilicate with an effective pore diameter of 3 Å and hollow porous spherical methyl methacrylate cross-polymer), slower diffusion of D_2O was successfully observed (Figure S6). These observations suggest that the spatiotemporal resolution of our analysis is high enough to discern diffusion differences of D_2O in cellular structures, if any. Therefore, we conclude that homogeneous diffusion patterns of D_2O observed in brain tissues under various conditions indeed reflect the truly homogeneous nature of brain tissues with regard to water diffusion.

Limitations of the study

We used acute brain slices to achieve an immediate exchange of extracellular solutions needed for characterization of water dynamics at high spatiotemporal resolution, and thus the potential roles of blood flow could not be assessed. In fact, previous studies have suggested a role of pulsation in the regulation of brain tissue water dynamics.[28] Thus, this study is not designed to test the conclusions of previous *in vivo* studies, including those of glymphatic systems or the potential roles of AQP4 in such a context.[15] Rather, as discussed above, the aim of our study was to reveal the intrinsic structural factors that define the dynamics of water and solutes in the brain; our findings clearly demonstrated the unique nature of water compared with solutes. Although technical difficulties are expected, including signal detection sensitivity and probe introduction, future studies should perform this type of multimodal multiphoton imaging to evaluate water dynamics *in vivo*, considering the roles of various physiological factors.

STAR★METHODS

Detailed methods are provided in the online version of this paper and include the following:

- KEY RESOURCES TABLE
- RESOURCE AVAILABILITY
  - Lead contact
  - Materials availability
  - Data and code availability
- EXPERIMENTAL MODEL AND STUDY PARTICIPANT DETAILS
- METHOD DETAILS
  - Materials
  - Spontaneous Raman scattering measurement
  - Brain slice preparations
  - Perfusion fixation and tissue clearing
  - Multimodal multiphoton imaging
  - Image analyses
  - Numerical simulations
- QUANTIFICATION AND STATISTICAL ANALYSIS

SUPPLEMENTAL INFORMATION

Supplemental information can be found online at https://doi.org/10.1016/j.crmeth.2023.100519.

ACKNOWLEDGMENTS

This study was supported by JSPS KAKENHI (20K20593, 20H02881), JST PRESTO (JPMJPR17G6), JST CREST (JPMJCR1872), JST-Mirai Program (JPMJMI22G5), and the Nakatani Foundation. We would like to thank Evident Corporation for their continuous technical support and Dr. Satoshi Ii (Tokyo Metropolitan University) for helpful discussions and scidraw.io for illustrations.

AUTHOR CONTRIBUTIONS

Conceptualization, T.S., M.Y., and M.N.; methodology, T.S., Y.O., and M.N.; software, T.S. and M.N.; validation, T.S. and M.N.; formal analysis, T.S. and

Figure 6. Dynamics of water and solutes under a pathological condition

(A–D) Representative images (A and B) and traces (C and D) of D_2O and Alexa Fluor 488 diffusion into brain slices before and after OGD (A and C) or in a control condition (B and D).

(E and F) Normalized intensity changes of D_2O and Alexa Fluor 488 under OGD (E) and the control condition (F).

(G and H) Summary data for D_2O (G; n.s., $p = 9.9 \times 10^{-1}$, Brunner-Munzel test) and Alexa Fluor 488 (H; *$p = 6.6 \times 10^{-3}$, Brunner-Munzel test) influx into brain slices under OGD and control conditions (control, n = 36 ROIs from six slices; OGD, n = 18 ROIs from six slices). See also Figure S3.

M.N.; investigation, T.S., T.M., K.K., and M.N.; resources, T.S., M.Y., and M.N.; data curation, T.S. and M.N.; writing – original draft, M.N.; writing – reviewing and editing, T.S., Y.O., M.Y., and M.N.; visualization, T.S. and M.N.; supervision, Y.O., M.Y., and M.N.; project administration, Y.O., M.Y., and M.N.; funding acquisition, Y.O., M.Y., and M.N.

DECLARATION OF INTERESTS

The authors declare no competing interests.

Received: December 12, 2022
Revised: April 26, 2023
Accepted: June 7, 2023
Published: June 29, 2023

REFERENCES

1. Benton, D., and Young, H.A. (2015). Do small differences in hydration status affect mood and mental performance? Nutr. Rev. *73* (*Suppl 2*), 83–96. https://doi.org/10.1093/NUTRIT/NUV045.
2. Schaefer, P.W., Grant, P.E., and Gonzalez, R.G. (2000). Diffusion-weighted MR imaging of the brain. Radiology *217*, 331–345. https://doi.org/10.1148/RADIOLOGY.217.2.R00NV24331.
3. MacAulay, N. (2021). Molecular mechanisms of brain water transport. Nat. Rev. Neurosci. *22*, 326–344.
4. Xiao, F., and Hrabetová, S. (2009). Enlarged extracellular space of aquaporin-4-deficient mice does not enhance diffusion of Alexa Fluor 488 or dextran polymers. Neuroscience *161*, 39–45. https://doi.org/10.1016/J.NEUROSCIENCE.2009.03.017.
5. Nuriya, M., Shinotsuka, T., and Yasui, M. (2013). Diffusion properties of molecules at the blood-brain interface: potential contributions of astrocyte endfeet to diffusion barrier functions. Cerebr. Cortex *23*, 2118–2126. https://doi.org/10.1093/cercor/bhs198.
6. Tønnesen, J., Inavalli, V.V.G.K., and Nägerl, U.V. (2018). Super-resolution imaging of the extracellular space in living brain tissue. Cell *172*, 1108–1121.e15. https://doi.org/10.1016/J.CELL.2018.02.007.
7. Yamakoshi, H., Dodo, K., Palonpon, A., Ando, J., Fujita, K., Kawata, S., and Sodeoka, M. (2012). Alkyne-tag Raman imaging for visualization of mobile small molecules in live cells. J. Am. Chem. Soc. *134*, 20681–20689. https://doi.org/10.1021/ja308529n.
8. Wei, L., Hu, F., Chen, Z., Shen, Y., Zhang, L., and Min, W. (2016). Live-cell bioorthogonal chemical imaging: stimulated Raman scattering microscopy of vibrational probes. Acc. Chem. Res. *49*, 1494–1502. https://doi.org/10.1021/acs.accounts.6b00210.
9. Nuriya, M., Ashikari, Y., Iino, T., Asai, T., Shou, J., Karasawa, K., Nakamura, K., Ozeki, Y., Fujimoto, Y., and Yasui, M. (2021). Alkyne-tagged dopamines as versatile analogue probes for dopaminergic system analysis. Anal. Chem. *93*, 9345–9355. https://doi.org/10.1021/acs.analchem.0c05403.
10. Oda, R., Shou, J., Zhong, W., Ozeki, Y., Yasui, M., and Nuriya, M. (2022). Direct visualization of general anesthetic propofol on neurons by stimulated Raman scattering microscopy. iScience *25*, 103936. https://doi.org/10.1016/j.isci.2022.103936.
11. Min, W., Freudiger, C.W., Lu, S., and Xie, X.S. (2011). Coherent nonlinear optical imaging: beyond fluorescence microscopy. Annu. Rev. Phys. Chem. *62*, 507–530. https://doi.org/10.1146/ANNUREV.PHYSCHEM.012809.103512.
12. Nuriya, M., Fukushima, S., Momotake, A., Shinotsuka, T., Yasui, M., and Arai, T. (2016). Multimodal two-photon imaging using a second harmonic generation-specific dye. Nat. Commun. *7*, 11557. https://doi.org/10.1038/ncomms11557.
13. Mizuguchi, T., Momotake, A., Hishida, M., Yasui, M., Yamamoto, Y., Saiki, T., and Nuriya, M. (2020). Multimodal multiphoton imaging of the lipid bilayer by dye-based sum-frequency generation and coherent anti-Stokes Raman scattering. Anal. Chem. *92*, 5656–5660. https://doi.org/10.1021/acs.analchem.0c00673.
14. Nuriya, M., Yoneyama, H., Takahashi, K., Leproux, P., Couderc, V., Yasui, M., and Kano, H. (2019). Characterization of intra/extracellular water states probed by ultrabroadband multiplex coherent anti-Stokes Raman scattering (CARS) spectroscopic imaging. J. Phys. Chem. A *123*, 3928–3934. https://doi.org/10.1021/acs.jpca.9b03018.
15. Iliff, J.J., Wang, M., Liao, Y., Plogg, B.A., Peng, W., Gundersen, G.A., Benveniste, H., Vates, G.E., Deane, R., Goldman, S.A., et al. (2012). A paravascular pathway facilitates CSF flow through the brain parenchyma and the clearance of interstitial solutes, including amyloid β. Sci. Transl. Med. *4*, 147ra111. https://doi.org/10.1126/scitranslmed.3003748.
16. Nimmerjahn, A., Kirchhoff, F., Kerr, J.N.D., and Helmchen, F. (2004). Sulforhodamine 101 as a specific marker of astroglia in the neocortex in vivo. Nat. Methods *1*, 31–37. https://doi.org/10.1038/nmeth706.
17. Shi, L., Zheng, C., Shen, Y., Chen, Z., Silveira, E.S., Zhang, L., Wei, M., Liu, C., de Sena-Tomas, C., Targoff, K., and Min, W. (2018). Optical imaging of metabolic dynamics in animals. Nat. Commun. *9*, 2995. https://doi.org/10.1038/s41467-018-05401-3.
18. Syková, E., and Nicholson, C. (2008). Diffusion in brain extracellular space. Physiol. Rev. *88*, 1277–1340. https://doi.org/10.1152/PHYSREV.00027.2007.
19. Nicholson, C., and Tao, L. (1993). Hindered diffusion of high molecular weight compounds in brain extracellular microenvironment measured with integrative optical imaging. Biophys. J. *65*, 2277–2290. https://doi.org/10.1016/S0006-3495(93)81324-9.
20. Gottschalk, A., Scafidi, S., and Toung, T.J.K. (2021). Brain water as a function of age and weight in normal rats. PLoS One *16*, e0249384. https://doi.org/10.1371/JOURNAL.PONE.0249384.
21. Espinosa, J.S., and Stryker, M.P. (2012). Development and plasticity of the primary visual cortex. Neuron *75*, 230–249. https://doi.org/10.1016/J.NEURON.2012.06.009.
22. Le Bihan, D., and Iima, M. (2015). Diffusion magnetic resonance imaging: what water tells us about biological tissues. PLoS Biol. *13*, e1002203. https://doi.org/10.1371/JOURNAL.PBIO.1002203.
23. Shinotsuka, T., Yasui, M., and Nuriya, M. (2014). Astrocytic gap junctional networks suppress cellular damage in an in vitro model of ischemia. Biochem. Biophys. Res. Commun. *444*, 171–176. https://doi.org/10.1016/j.bbrc.2014.01.035.
24. Ibata, K., Takimoto, S., Morisaku, T., Miyawaki, A., and Yasui, M. (2011). Analysis of aquaporin-mediated diffusional water permeability by coherent anti-Stokes Raman scattering microscopy. Biophys. J. *101*, 2277–2283. https://doi.org/10.1016/J.BPJ.2011.08.045.
25. MacAulay, N. (2021). Molecular mechanisms of brain water transport. Nat. Rev. Neurosci. *22*, 326–344. https://doi.org/10.1038/s41583-021-00454-8.
26. Hama, H., Hioki, H., Namiki, K., Hoshida, T., Kurokawa, H., Ishidate, F., Kaneko, T., Akagi, T., Saito, T., Saido, T., and Miyawaki, A. (2015). ScaleS: an optical clearing palette for biological imaging. Nat. Neurosci. *18*, 1518–1529. https://doi.org/10.1038/nn.4107.
27. Alshuhri, M.S., Gallagher, L., Work, L.M., and Holmes, W.M. (2021). Direct imaging of glymphatic transport using H217O MRI. JCI Insight *6*, e141159. https://doi.org/10.1172/jci.insight.141159.
28. Iliff, J.J., Wang, M., Zeppenfeld, D.M., Venkataraman, A., Plog, B.A., Liao, Y., Deane, R., and Nedergaard, M. (2013). Cerebral arterial pulsation drives paravascular CSF-interstitial fluid exchange in the murine brain. J. Neurosci. *33*, 18190–18199. https://doi.org/10.1523/JNEUROSCI.1592-13.2013.
29. Mizuguchi, T., Nuriya, M., Yasui, M., Iino, T., Ozeki, Y., and Saiki, T. (2021). Sensitive detection of alkyne-terminated hydrophobic drug by surface-enhanced stimulated Raman scattering in cetyltrimethylammonium bromide-coated gold nanorod suspensions. Appl. Phys. Express *14*, 032003. https://doi.org/10.35848/1882-0786/abdfa3.

30. Mudalige, A., and Pemberton, J.E. (2007). Raman spectroscopy of glycerol/D2O solutions. Vib. Spectrosc. *45*, 27–35. https://doi.org/10.1016/J.VIBSPEC.2007.04.002.

31. Abramczyk, H., Brozek-Pluska, B., Krzesniak, M., Kopec, M., and Morawiec-Sztandera, A. (2014). The cellular environment of cancerous human tissue. Interfacial and dangling water as a "hydration fingerprint. Spectrochim. Acta Mol. Biomol. Spectrosc. *129*, 609–623. https://doi.org/10.1016/j.saa.2014.03.103.

32. Ikeshima-Kataoka, H., Abe, Y., Abe, T., and Yasui, M. (2013). Immunological function of aquaporin-4 in stab-wounded mouse brain in concert with a pro-inflammatory cytokine inducer, osteopontin. Mol. Cell. Neurosci. *56*, 65–75. https://doi.org/10.1016/J.MCN.2013.02.002.

33. Schindelin, J., Arganda-Carreras, I., Frise, E., Kaynig, V., Longair, M., Pietzsch, T., Preibisch, S., Rueden, C., Saalfeld, S., Schmid, B., et al. (2012). Fiji: an open-source platform for biological-image analysis. Nat. Methods *9*, 676–682. https://doi.org/10.1038/nmeth.2019.

34. Okabe, M., Ikawa, M., Kominami, K., Nakanishi, T., and Nishimune, Y. (1997). Green mice'' as a source of ubiquitous green cells. FEBS Lett. *407*, 313–319. https://doi.org/10.1016/S0014-5793(97)00313-X.

35. Pnevmatikakis, E.A., and Giovannucci, A. (2017). NoRMCorre: an online algorithm for piecewise rigid motion correction of calcium imaging data. J. Neurosci. Methods *291*, 83–94. https://doi.org/10.1016/J.JNEUMETH.2017.07.031.

36. Stringer, C., Wang, T., Michaelos, M., and Pachitariu, M. (2021). Cellpose: a generalist algorithm for cellular segmentation. Nat. Methods *18*, 100–106. https://doi.org/10.1038/s41592-020-01018-x.

STAR★METHODS

KEY RESOURCES TABLE

REAGENT or RESOURCE	SOURCE	IDENTIFIER
Chemicals, peptides, and recombinant proteins		
Deuterium oxide	Sigma-Aldrich	435767
Alexa Fluor™ 488 Carboxylic Acid, tris(triethylammonium) salt	Thremo Fisher Scientific	A33077
Dextran, Alexa Fluor™ 488; 10,000 MW, Anionic, Fixable	Thremo Fisher Scientific	D22910
Molecular Sieves 3A 1/8	nacalai tesque	04177-45
MATSUMOTO MICROSPHERE MHB-R	Matsumoto Yushi-Seiyaku	N/A
SCALEVIEW-S Trial Kit	FUJIFILM Wako Pure Chemical	299-79901
Phalloidin-iFluor 488 Reagent	Abcam	ab176753
FG beads	TAMAGAWA SEIKI	TAS8848N1161
Experimental models: Organisms/strains		
Mouse: C57BL/6-Tg C14-Y01-FM131Osb	RIKEN BRC	RBRC00267
Mouse: Aqp4 null mice	Ikeshima-Kataoka et al.[32]	
Software and algorithms		
MATLAB R2020b, R2021b	Mathworks	RRID:SCR_001622
Fiji (Image J)	Schindelin et al.[33]	RRID:SCR_002285
R 4.2.0	The R Foundation	RRID:SCR_001905
RStudio 2022.02.3	RStudio	RRID: SCR_000432
Python 3.8.12	Python	RRID:SCR_008394
Origin Pro 2021	OriginLab	RRID:SCR_014212

RESOURCE AVAILABILITY

Lead contact

Further information and requests for resources and reagents should be directed to and will be fulfilled by the lead contact, Mutsuo Nuriya (mnuriya@keio.jp).

Materials availability

This study did not generate new unique reagents.

Data and code availability

- All data reported in this paper will be shared by the lead contact upon request.
- All original code is available in this paper's supplemental information.
- Any additional information required to reanalyze the data reported in this paper is available from the lead contact upon request.

EXPERIMENTAL MODEL AND STUDY PARTICIPANT DETAILS

Mice were housed in a 12-hour light dark cycle with *ad libitum* access to food and water. All procedures related to the care and treatment of animals were approved by the Keio University Institutional Animal Care and Use Committee. 2–4-week-old C57BL/6J mice (wild type or AQP4 knockout) of either sex were used in this study; sex was not considered as a factor to influence results and data are presented as summary of all animals used regardless of sex.

METHOD DETAILS

Materials

Chemicals were purchased from Sigma Aldrich Japan (Tokyo, Japan), unless otherwise stated.

Spontaneous Raman scattering measurement

Spontaneous Raman scattering spectra were obtained using a spectroscopic module (Hamamatsu Photonics C15471, Shizuoka, Japan). D_2O in the cuvette was illuminated with a 50-mW 785-nm laser, and the resulting Raman scattering signals were collected. The data were analyzed using Origin Pro, and an FFT low-pass filter was applied to the obtained data to cancel high frequency noise.

Brain slice preparations

In all experiments using mice, procedures related to the care and treatment of animals were approved by the Keio University Institutional Animal Care and Use Committee. Brain slices were prepared as previously described.[5] Briefly, 2–4-week-old C57BL/6J mice of either sex (Japan SLC, Shizuoka, Japan) were anesthetized using isoflurane and decapitated, after which their brains were quickly removed and placed in ice-cold cutting solution containing 222 mM sucrose, 27 mM $NaHCO_3$, 2.6 mM KCl, 1.5 mM NaH_2PO4, 0.5 mM $CaCl_2$, and 7 mM $MgCl_2$; the solution was bubbled with 95% O_2/5% CO_2 at pH 7.4. Coronal brain slices (300 μm thick) were prepared using a Leica VT1200S Microtome (Leica Microsystems, Wetzlar, Germany) in the ice-cold cutting solution. The slices were then transferred to artificial cerebrospinal fluid (aCSF) containing 126 mM NaCl, 3 mM KCl, 1.14 mM NaH_2PO_4, 26 mM $NaHCO_3$, 3 mM $CaCl_2$, 1 mM $MgCl_2$, and 10 mM dextrose; the aCSF was pre-warmed to 37°C, bubbled with 95% O_2/5% CO_2 at pH 7.4, and incubated for 30 min for recovery before being cooled to room temperature (approximately 22°C) prior to use. For astrocyte imaging, brain slices were loaded with 200 nM SR101 during the recovery period.[5] For OGD experiments, the solution was changed from normal aCSF to OGD aCSF, in which the glucose had been replaced with 10 mM of sucrose and the solution had been bubbled with 95% N_2/5% CO_2.

CAG-EGFP mice (C57BL/6-Tg C14-Y01-FM131Osb) were used in some experiments. These mice express EGFP under the control of the CAG promoter (CMV-IE enhancer, chicken beta-actin promoter, rabbit beta-globin genomic DNA).[34] Mice were obtained from the RIKEN BioResource Research Center and maintained as homozygotes. Similarly, AQP4 knockout animals[32] were maintained as homozygotes and used as other animals. In experiments comparing SRS signals at 3,400 cm^{-1} and 2,900 cm^{-1}, fixed brain slices prepared from wild-type animals were stained with Phalloidin-iFluor-488 (Abcam, Cambridge, UK) for 1 hr at room temperature before imaging.

Perfusion fixation and tissue clearing

In some experiments, perfusion-fixed brain tissue was used. Briefly, mice were anesthetized with isoflurane, and cardiac perfusion was performed with phosphate-buffered saline (PBS), followed by 4% paraformaldehyde (PFA)/PBS (Nacalai Tesque, Kyoto, Japan). The brain tissue was removed and post-fixed in 4% PFA/PBS for 2–7 days at 4°C. Coronal brain slices were prepared using a microtome, as described above.

Tissue clearing was performed using a SCALEVIEW S kit (FUJIFILM Wako Pure Chemical, Osaka, Japan), based on a previously published protocol.[26] Briefly, brain slices were sequentially incubated with solutions SCALEVIEW S0 to S3 solutions for 30 min each at 37°C, followed by incubation in deSca*l*e solution at 4°C for 30 min twice. Subsequently, the brain slices were incubated in solution S4 overnight at 37°C, followed by incubation in a mounting solution for 60 min at 37°C. The brain slices were kept in the mounting solution at 4°C until microscopic observation. Imaging was performed in the Sca*l*e mounting solution supplied in the SCALEVIEW kit.

Multimodal multiphoton imaging

The multimodal multiphoton system was essentially the same as that we previously reported.[10,29] Briefly, a Yb-fiber-based picosecond laser (Emerald Engine, Angewandte Physik & Elektronik GmbH, APE, Berlin, Germany) was used as the laser source. The fundamental 1,032-nm laser was used directly as a Stokes beam, whereas a simultaneously emitted second-harmonic 516-nm laser was fed to an optical parametric oscillator (APE) to change the wavelength of the laser to be used as a pump beam, such that the wavenumber difference between the pump and Stokes beams matched the vibration energy of O-D at 2,400 – 2,450 cm^{-1}.[30,31] The intensity of the Stokes beam was modulated by an electro-optical modulator (Thorlabs, New Jersey, U.S.A.), such that the intensities of the Stokes beam changed repetitively in every other pulse of the pump beam emitted at 76 MHz.

The pulse timings of the pump and Stokes beams were matched using a delay line in the Stokes light path. These beams were merged through a dichroic mirror and circularly polarized through an achromatic quarter-wave plate (Thorlabs). The beams were then scanned using a galvo-galvo mirror (Thorlabs) and focused on the samples using a 25× objective lens designed for multiphoton microscopy (Olympus, NA 1.05, Tokyo, Japan). The laser power used for SRS imaging was 75–125 mW for both the pump and Stokes beams at the objective lens. The transmitted light was collected using another 25× objective lens (Olympus, NA 1.05) placed on the other side of the sample. The transmitted pump beam was detected using a photodiode, and the SRS signal was extracted using a custom-made lock-in amplifier. Fluorescent signals were captured by the illuminating objective lens and collected via photomultiplier tubes (Thorlabs) after band-pass filters (520–550 nm for green and 580–620 nm for red). Optical signals were fed into the computer after an A/D converter (National Instruments PCIe-6376, Texas, U.S.A.), and imaging was performed using ScanImage 2021 (Vidrio Technologies, Virginia, U.S.A.) run on the MATLAB platform (MathWorks, Massachusetts, U.S.A.). The full field of view of the imaging system was 419 μm × 419 μm, and zooming was performed in individual experiments. The pixel dwell time was 3.2 μsec and the frame rate was 1.07 Hz.

Brain slices were placed in a perfusion chamber (Warner Instruments, Massachusetts, U.S.A.) and oxygenated aCSF was continuously perfused during imaging. To track the dynamics of water, aCSF was changed from normal aCSF to aCSF containing 20% D_2O

and 1 – 50 μM fluorescent molecules (Alexa Fluor 488 carboxylic acid or Alexa Fluor 488 conjugated with 10 kDa dextran, Thermo Fisher, Massachusetts, U.S.A.). The osmolality of the solutions was measured using a vapor pressure osmometer (YSI VAPRO 5520, Xylem Japan, Kanagawa, Japan). Differences in osmolality between H_2O- and D_2O-based aCSF were negligible, if any (H_2O aCSF, 309.6 ± 3.1 mOsm, n = 12; D_2O aCSF, 307.6 ± 3.4 mOsm, n = 12; H_2O OGD aCSF, 310.5 ±1.5 mOsm, n = 6; D_2O OGD aCSF, 311.2 ±2.4 mOsm, n = 6; mean ± SEM). To image D_2O and Alexa Fluor dye influxes, 10 min of time-lapse imaging was performed with normal aCSF influx recording in the initial ~1 min, followed by Alexa Fluor-containing D_2O aCSF influx recording. During the time-lapse imaging, drifts along the z-axis were manually corrected based on a SR101 reference image in individual experiments. All measurements were performed at room temperature to avoid potential experimental artefacts resulting from evaporation of water and concomitant changes in osmolarity by heating.

To calculate the concentration dependency of the D_2O and H_2O SRS signals, water samples containing various concentrations of D_2O and H_2O were prepared and measured directly. The spatial resolution of the SRS system was estimated by measuring the SRS signals of subresolution-sized alkyne beads (diameter 180 ± 30 nm, Tamagawa Seiki, Nagano, Japan) mounted on a glass slide using Prolong Glass Antifade Mountant (Thermo Fisher) at 2,100 cm^{-1}. To evaluate the sensitivity of the imaging system to discern different water dynamics in the field of view, two materials expected to have slower water diffusion were employed: 1) small pieces of molecular sieves 3A (synthetic crystalline aluminosilicate with an effective pore diameter of 3 Å, Nacalai Tesque) and 2) hollow porous spherical methyl methacrylate crosspolymer with an 8–25 μm diameter (MATSUMOTO MICROSPHERE MHB-R, kind gift from Matsumoto Yushi-Seiyaku, Osaka, Japan). These materials were embedded in 2% agarose gel and the same diffusion analysis was performed in the same manner as for brain slices.

Image analyses

The imaging data were analyzed using custom-written codes in MATLAB (R2020b and R2021b, Supplementary Codes). Motion correction of the time-series SR101 images was performed using the NoRMCorre algorithm.[35] The calculated motion corrections were applied to other simultaneous acquired time-series images using the "apply_shifts" function in MATLAB. Nine to 15 regions of interest (ROIs, 50 × 50 pixels) in individual experiments were manually selected at random using ImageJ Fiji (National Institute of Health, U.S.A.). In higher-magnification experiments, ROIs inside cells were selected automatically using the Cellpose algorithm.[36] ROIs outside cells were manually selected by converting the ROIs inside cells to a square using ImageJ Fiji based on fluorescence tracer signals.

To analyze the time-series signal of D_2O SRS and Alexa Fluor 2PE, the signal intensity of each signal in each ROIs was first averaged in each frame. The mean time-series signal intensity was smoothed by a "smoothdata" function in MATLAB using the following parameters: method = sgolay, degree = 2, and smoothing window = 15. After normalizing the smoothed traces, the time of each signal increase in the individual ROIs was determined by applying the "findchangepts" function in MATLAB using the following parameters: Statistic = linear and MaxNumChanges = 10. The output of the function that was closest to the time to reach the perfusion chamber (~80 s) from the beginning of each imaging experiment was regarded as the time of the signal increase. The approximately 4-min normalized traces (from the time of increase to 350th frame, except for the OGD experiments where the time of increase to 300th frame was used to exclude artificial signal changes due to severe focus shifts) were fitted using a single exponential function as follows:

$$I(t) = Imax\left\{1 - \exp\left(-\frac{t}{\tau}\right)\right\} + \varepsilon$$

Where I indicates the signal intensity, t indicates the time points, and τ indicates the time constant. ROIs with adjusted $R^2 < 0.80$ were excluded from subsequent analyses.

Normalized intensities were calculated as follows. First, averaged signal intensity at the beginning of experiments (1–50 frames) in each ROI was subtracted at the end of fitting. Next, subtracted values in ROIs inside brain tissue were divided by those in ROIs outside brain tissue, representing the free diffusion of water and fluorescence dyes. In experiments assessing spatial distributions of D_2O and Alexa Fluor (Figure 4), signal intensities in ROIs inside and outside cells were divided by average values of the entire imaging plane. In the OGD experiments (Figure 6), relative intensities were calculated by normalizing intensities 30 min after the control/OGD solution by values before control/OGD initiation.

Numerical simulations

Numerical simulations of the signal intensities were performed using custom-written codes in MATLAB (Supplementary Codes). In these simulations, 100 μm lateral × 100 μm axial observation area (xz plane) with 0.25 μm × 0.25 μm pixel size was defined with various diameters of a cell placed in the middle of the field of view. To evaluate how much of the signal in the areas outside the cell comes to the field inside the cell, the true signal intensities outside and inside the cell were set to 1 and 0, respectively. Assuming a Gaussian distribution of the point-spread function with FWHM experimentally measured on both the lateral and axial axes, the observed signal intensities in each pixel were calculated by integrating signals coming from all pixels in the whole field with the contribution factors calculated below.

$$\left\{\frac{1}{w_{lateral}\times\sqrt{\frac{\pi}{2}}}\times e^{-2\times\left(\frac{x-x_0}{w_{lateral}}\right)^2}\right\}\times\left\{\frac{1}{w_{axial}\times\sqrt{\frac{\pi}{2}}}\times e^{-2\times\left(\frac{z-z_0}{w_{axial}}\right)^2}\right\}$$

where w is the width factor calculated from FWHM by FWHM $\times\sqrt{\log 4}$ and (x_0, z_0) is the position of the observation point. Calculated "observed" signal intensities were normalized to the maximum values in the field (outside the cell).

QUANTIFICATION AND STATISTICAL ANALYSIS

To test for statistical significance, the non-parametric two-sided Brunner-Munzel test (R 4.2.0) and Wilcoxon signed-rank test were used for independent and paired samples, respectively. No statistical methods were used to determine the sample size and no data were excluded from analyses.

In box plots, the box represents the 25th, 50th, and 75th percentile lines, and whiskers show the maximum and minimum points excluding outliers defined by points outside of the 1.5 × inter-quartile range. Paired data are connected by lines.